Supporting Information

Structural Variability in Transition Metal Oxide Clusters:

Gas Phase Vibrational Spectroscopy of $V_3O_{6-8}^+$

Knut R. Asmis,*[a,b] Torsten Wende,[a] Mathias Brümmer,[b] Oliver Gause,[b] Gabriele Santambrogio,[a,b] E. Cristina Stanca-Kaposta,[b] Jens Döbler,[c] Andrzej Niedziela[c] and Joachim Sauer*[c]

[a] *Fritz-Haber-Institut der Max-Planck-Gesellschaft, Faradayweg 4-6, D-14195 Berlin, Germany. Fax: 49 30 8413-5603; Tel: 49 30 8413-5735; E-mail: asmis@fhi-berlin.mpg.de*

[b] *Institut für Experimentalphysik, Freie Universität Berlin, Arnimallee 14, D-14195 Berlin, Germany.*

[c] *Institut für Chemie, Humboldt-Universität Berlin, Unter den Linden 6, D-10099 Berlin, Germany. Fax: 49 30 2093-7136; Tel: 49 30 2093-7134; E-mail: js@chemie.hu-berlin.de*

1. Computational details for wavefunction based calculations

For the $V_3O_8^+$ η^2-peroxo cage and η^2-superoxo cage structures wavefunction based calculations were performed as single point calculation at the B3LYP/TZVP structures with MOLPRO 2006.[1] Coupled cluster calculations with single and double substitution and pertubative treatment of triple substitutions (CCSD(T))[2] were performed with a restricted singlet closed shell Hartree-Fock reference function. In both cases high T1 diagnostic values (peroxo: 0.06. superoxo: 0.08) indicate limited applicability of such a single reference method.

Additionally. multireference calculations were performed in the following way: Starting from the restricted singlet closed shell Hartree-Fock solution a CASSCF[3] calculation with an active space of 4 electrons in 4 orbitals was performed. In each irreducible representation the HOMO and the LUMO were included in the active space. An analysis of the CASSCF orbitals showed that the active space corresponds to a superposition of the π^* orbitals of the O_2 moiety and a vanadium d-orbital. The CAS was then extended to 8 electrons in 8 orbitals by adding the O_2 π orbitals and the lowest unoccupied orbitals. The resulting CASSCF orbitals were checked again to confirm. that the solution corresponds to O_2 π and π^* orbitals in the active space. In both cases significant multireference character was found. as evidenced by rather small C_0 values (peroxo: 0.896. superoxo: 0.849). Finally. dynamic correlation was added in terms of Rayleigh-Schrödinger perturbation theory of second order (module RS2C)[4].

References

1 H.-J. Werner. P. J. Knowles. R. Lindh. F. R. Manby. P. C. M. Schütz. T. Korona. G. Rauhut. R. D. Amos. A. Bernhardsson. A. Berning. D. L. Cooper. M. J. O. Deegan. A. J. Dobbyn. F. Eckert. C. Hampel. G. Hetzer. A. W. Lloyd. S. J. McNicholas. W. Meyer. M. E. Mura. A. Nicklaß. P. Palmieri. R. Pitzer. U. Schumann. H. Stoll. A. J. Stone.R. Tarroni and T. Thorsteinsson. MOLPRO package of *ab initio* programs. 2006.

2 C. Hampel. K. A. Peterson and H. J. Werner. *Chem. Phys. Lett.*. 1992. **190**. 1–12; M. J. O. Deegan and P. J. Knowles. *Chem. Phys. Lett.*. **227**. 1994. 321-326.

3 H.-J. Werner and P. J. Knowles. *J. Chem. Phys.*. 1985. **82**. 5053-5063; P. J. Knowles and H.-J. Werner. *Chem. Phys. Lett.*. **115.** 1985. 259-267.

4 H.-J. Werner. *Mol. Phys.*. 1996. **89**. 645-661; P. Celani and H.-J. Werner. *J. Chem. Phys.*. 2000. **112**. 5546-5557.

Table S1: Total B3LYP/TZVP energies (Hartree) of most stable $V_3O_6^+$ and $V_3O_7^+$ isomers as well as their He and Ar complexes, respectively. In parenthesis: B3LYP+D energies.

Isomer		State	E	Complex	State	E
He			-2.90591			
$V_3O_6^+$	Chain	C_2-^{3}B	-3283.169575 (-3283.17637)	He-He	C_2-^{3}B	-3288.98864 (3288.99669)
Ar			-527.479313			
$V_3O_7^+$	Cage	C_{3v}-$^1A_1$	-3358.393467 (-3358.404607)	Ar	C_s-^{1}A’	-3885.878729 (-3885.892703)

Table S2: Total B3LYP/TZVP energies (Hartree) of $V_3O_8^+$ isomers[a] and their Ar complexes. In parenthesis: B3LYP+D energies.

Isomer	State	$V_3O_8^+$ E+3433	State[a]	$V_3O_8^+$·Ar E+3961
η^2-Peroxo-Cage	C_s-^{1}A‘	-0.537822 (-0.550556)	C_s-^{1}A‘	-0.020780 (-0.036898)
η^2-Superoxo-Cage	C_1-^{bs}A	-0.539537	C_1-^{bs}A	-0.023193
			C_1-^{bs}A	-0.022834
η^2-Superoxo-Chain-a	^{3}A	-0.535511		
η^2-Superoxo-Chain-b	^{3}A	-0.534533		
η^2-Superoxo-Cage-a	^{3}A	-0.533401		
η^2-Superoxo-Ring	C_{2v}-$^3A_2$	-0.532697	C_s-^{3}A”	-0.018838
			C_s-^{bs}A’	-0.013798
η^2-Peroxo-Ring	C_{2v}-$^1A_2$	-0.531681 (-0.547170)	C_s-^{1}A’	-0.019090 (0.038049)
η^2-Superoxo-Ring’	C_1-^{3}A	-0.530452	C_1-^{3}A	-0.018838
η^2-Peroxo-Cage/Ring-TS	C_s-^{1}A‘	0.529354 (-0.544162)	C_s-^{1}A‘	-0.015671 (-0.033269)
η^2-Superoxo-Cage-b	^{3}A	-0.527958	^{3}A	
η^2-Superoxo-Cage	C_s-^{3}A‘	-0.527331	C_s-^{3}A‘	
μ-(η^1-η^1)-Peroxo-Ring-a	C_s-^{1}A'	-0.527296	C_s-^{1}A'	-0.025676
μ-(η^1-η^1)-Peroxo-Ring-b	C_s-^{1}A'	-0.524007	C_s-^{1}A'	-0.022513
μ-(η^1-η^2)-Peroxo-Cage	C_1-^{1}A	-0.525987	C_1-^{1}A	-0.012518
			C_1-^{1}A	-0.011642
η^2-Superoxo-Cage	C_1-^{3}A	-0.524742	C_1-^{3}A	
μ-(η^2-η^2)-Peroxo-Cage	C_s-^{1}A'	-0.524383	C_s-^{1}A'	
μ-(η^1-η^1)-Peroxo-Cage	C_s-^{1}A'	-0.523968	C_s-^{1}A'	-0.010266
μ-(η^2-η^2)-Peroxo-Ring	C_1-^{1}A	-0.523070	C_1-^{1}A	-0.017656
μ^3-(η^1-η^1-η^1)-Peroxo-Ring	C_s-^{1}A'	-0.521504	C_s-^{1}A'	
μ^3-(η^1-η^1-η^2)-Peroxo-Cage	C_s-^{1}A'	-0.520930	C_s-^{1}A'	
μ-(η^2-η^1)-Peroxo-Ring	C_1-^{1}A	-0.517707	C_1-^{1}A	-0.012100
μ-(η^1-η^1)-Peroxo-Ring	C_1-^{1}A	-0.516022	C_1-^{1}A	-0.014130
η^2-Superoxo-Ring-2up	C_1-^{3}A	-0.515808	C_1-^{3}A	
η^2-peroxo-Ring	C_1-^{1}A	-0.515615	C_1-^{1}A	-0.012991

[a] bs - broken symmetry, mixture of open shell singlet and triplet spin states

Table S3: Relative stability of $V_3O_8^+$ isomers[a] and their Ar complexes (kJ/mol) predicted by B3LYP/TZVP. ΔE is the binding energy of Ar atoms to $V_3O_8^+$, R the Ar-V distance in pm. Energies in parenthesis are B3LYP+D results.

	$V_3O_8^+$			$V_3O_8^+ \cdot Ar$			
Isomer	State[b]	R_{O-O}	E	State[b]	E	R	ΔE
η^2-peroxo cage	C_s-$^1A'$	140	0[a] (0)	C_s-$^1A'$	12.9 (21.0)	296	9.6 (18.6)
				C_1-^1A	9.1 (18.7)		13.3 (20.8)
η^2-superoxo cage-a	C_1-^{bs}A	133	-4.5 (-3.7)		6.5 (16.8)	285	11.4 (19.1)
					7.5	295	10.5
η^2-superoxo chain-a	C_1-^3A	130	6.1				
η^2-superoxo chain-b	C_1-^3A	130	8.6				
η^2-superoxo cage-b	C_1-^3A	130	11.6		10.8	267	23.2
η^2-superoxo ring	C_{2v}-$^3A_2$	130	13.5	$^3A''$	31.2	320	4.7
η^2-superoxo ring				$^{bs}A'$	18.0	264	17.9
η^2-peroxo ring	C_{2v}-$^1A_2$	142	16.1 (8.8)		17.3 (17.6)	267	21.3 (30.8)
η^2-superoxo ring-2	C_1-^3A	130	19.3		18.0	270	23.8
η^2-superoxo cage-a	C_1-^3A	131	25.9				
η^2-superoxo cage	C_s-$^3A'$	130	27.5				
μ-(η^1-η^1)-peroxo ring-a	C_s-$^1A'$	141	27.6 (15.1)		0 (0)	253	50.1 (54.7)
μ-(η^1-η^1)-peroxo ring-b	C_s-$^1A'$	141	36.3 (24.0)		8.3	253	50.4
μ-(η^1-η^2)-peroxo cage	C_1-^1A	142	31.1		34.5	273	19.0
η^2-superoxo cage-TS	C_s-$^3A''$	130	41.2		36.8	276	16.7
η^2-superoxo ribbon	C_1-^3A	130	34.3				
μ-(η^2-η^2)-peroxo cage	C_s-$^1A'$	144	35.3				
μ-(η^1-η^1)-peroxo cage	C_s-$^1A'$	140	36.4		40.5	275	18.3
μ-(η^2-η^2)-peroxo ring	C_1-^1A	146	38.7 (29.6)		21.1 (20.6)	258	40.1 (48.5)
μ^3-(η^1-η^1-η^1)-peroxo ring	C_s-$^1A'$	147	42.8				
μ^3-(η^1-η^1-η^2)-peroxo cage	C_s-$^1A'$	144	44.3				
μ-(η^2-η^1)-peroxo ring	C_1-^1A	144	52.8		35.6	259	39.6
μ-(η^1-η^1)-peroxo ring	C_1-^1A	138	57.2		30.3	254	49.4
η^2-superoxo ring-2up	C_1-^3A	130	57.8				
η^2-peroxo ring	C_1-^1A	139	58.3		33.3	254	47.4

[a] Binding energy is 121.1 kJ/mol (with respect to $V_3O_6^+ + O_2$) or – 43.9 kJ/mol (with respect to $V_3O_7^+ + ½\ O_2$). The binding energy of ½ O_2 is 250.6 kJ/mol.

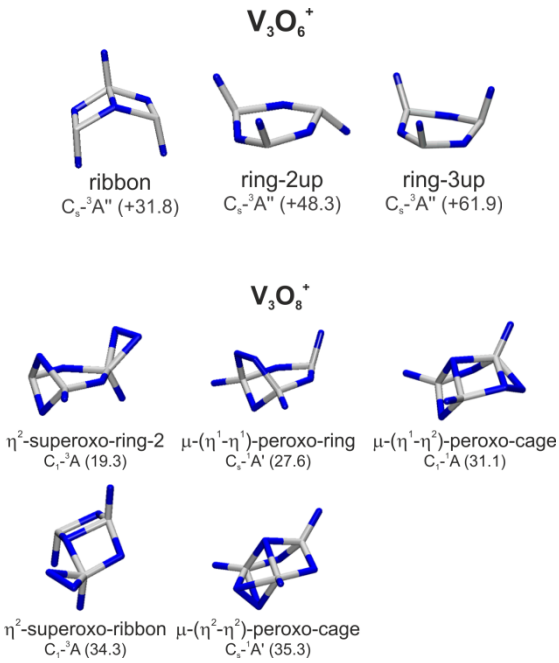

Figure S1: Additional B3LYP/TZVP structures of $V_3O_6^+$ and $V_3O_8^+$ isomers. Relative energies (kJ/mol) with respect to the most stable species are stated in parenthesis.

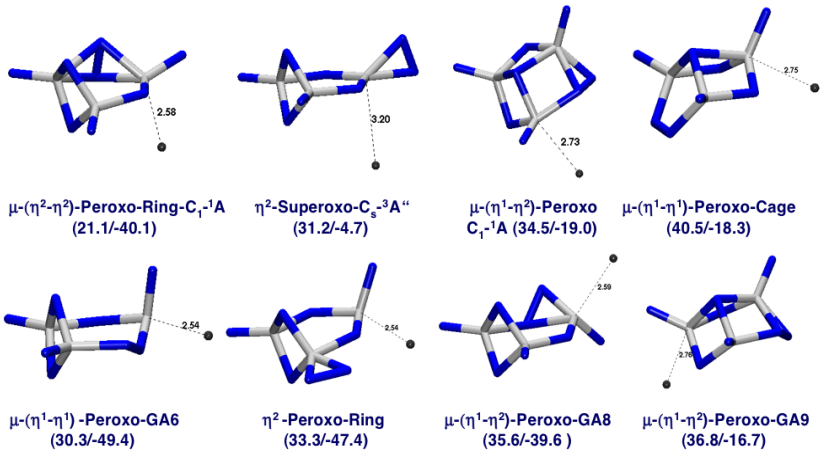

Figure S2: Additional $V_3O_8^+$Ar isomers. B3LYP/TZVP structures. In parenthesis (kJ/mol): relative energies with respect to the most stable species and Ar binding energies with respect to the bare cation.

2. Experimental details

Photodissociation cross section and normalized parent ion yield

IRPD spectra are generated from the TOF-data measured as a function of the irradiation wavenumber. A time window Δt_i is defined for each mass channel i and the wavenumber-dependent ion yield $I_i'(\nu)$ is determined by integration and then normalized to the total ion signal in order to cancel out fluctuations in the source conditions.

$$I_i\ (\upsilon) = I_i'(\upsilon)/\sum_j^{all\ ions} I_j'(\upsilon) \qquad (1)$$

The photodissociation cross sections σ is determined from the normalized parent ion yield $I(\nu)$ and the frequency dependent laser power $P(\nu)$ using:

$$\sigma = -ln[I(\upsilon)]/P(\upsilon)\ . \qquad (2)$$

The normalized parent ion yield $I(\nu)$ may refer to a single mass channel or also the sum of a range of mass channels.

$$I(\upsilon) = \frac{\sum_j^{parent\ \ ions} I_j\ (\upsilon)}{I_0} \qquad (3)$$

I_0 corresponds to the parent ion yield without the laser applied (i.e., no photodissociation).

Definition of parent and fragment ion mass channels

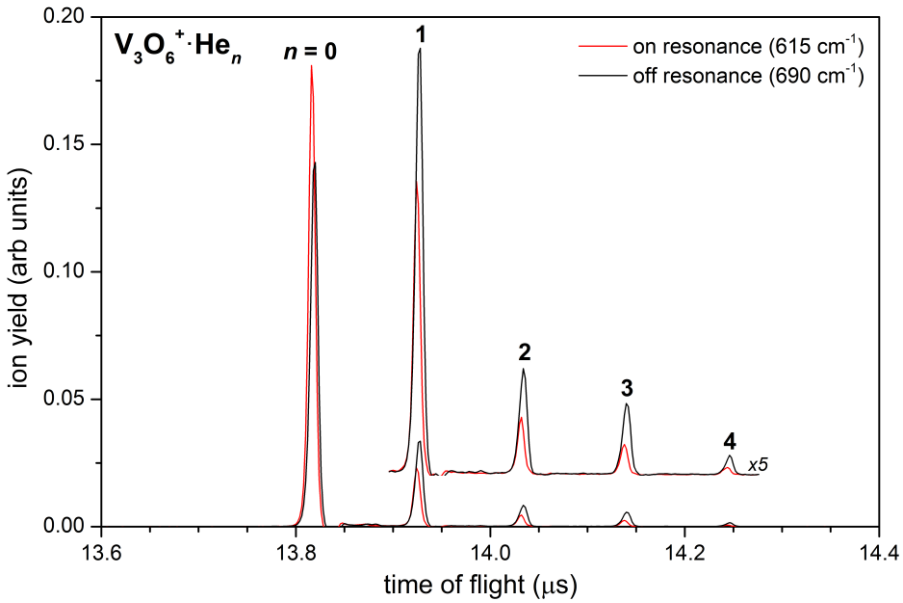

Figure S3: Time-of-flight (TOF) mass spectrum of $V_3O_6^+ \cdot He_n$ complexes after irradiation by IR laser pulse. The two traces correspond to the ion yield, when the laser wavenumber is tuned on (red) and off (black) resonance with the vibrational transition around 615 cm^{-1} (see also Fig. S4).

Mass-selected $V_3O_6^+$ ions are trapped in the ion trap and $V_3O_6^+ \cdot He_n$ complexes are formed by three-body collisions. A distribution is formed ranging from n=0 to n=4 (See Fig. S3). *All* of these ions are extracted from the ion trap, focused, and irradiated by the IR laser pulse, leading to the observed depletion of the n>0 peaks (and formation of the n=0 ion), when on resonance with a vibrational transition (see Fig. S3).

Ideally, one would like to measure IRPD spectra of each $V_3O_6^+ \cdot He_n$ complex with n=0-4 individually. Currently, we cannot do this. In the present experiments multiple ions of different mass ($V_3O_6^+ \cdot He_n$ with n=0-4) are present leading to the possibility of "cross-talk" between the different dissociation channels. For example, the n=2 mass channel may contain contributions from both parent as well as fragment ions, i.e., the n=2 complex can dissociate into lighter species (n=0,1) and it can be formed by dissociation of the heavier complexes (n=3,4). This makes the distinction of ion signals into parent and fragments ion signals ambiguous, except for n=4, which is always only parent ion, since it is the largest complex formed (see Fig. S3).

One strategy to simply things is to define all mass channels of the complexes (n=1-4) as "parent" ion channels and to sum the corresponding ion yields (see equation 3 on p. S5). This yields spectrum **F** in Fig. S4, in which effectively only those dissociation processes are considered, in which all He atoms are lost and bare $V_3O_6^+$ (n=0) is formed. In other words, dissociation processes leading to fragments with n>0 are cancelled out in spectrum **F**. One can also determine the IRPD spectra for all other mass channels individually (spectra **B**-**D** in Fig. S4). The fact that spectrum D (n=1) and F (n=1-4) are very similar suggests that under the present experimental conditions loss of all He atoms for the larger complexes (n>1) is favored. Further evidence for this is the absence of negative values for the cross section in the spectra **B**-**D**, which would signal that for this particular mass channel more ions are formed than depleted. Consequently, the "cross-talk" in-between the n=1 to n=3 channels is negligible and the spectra B-D in Figure S4 reflect the IRPD spectra of the individual (mass-selected) complexes probably quite well.

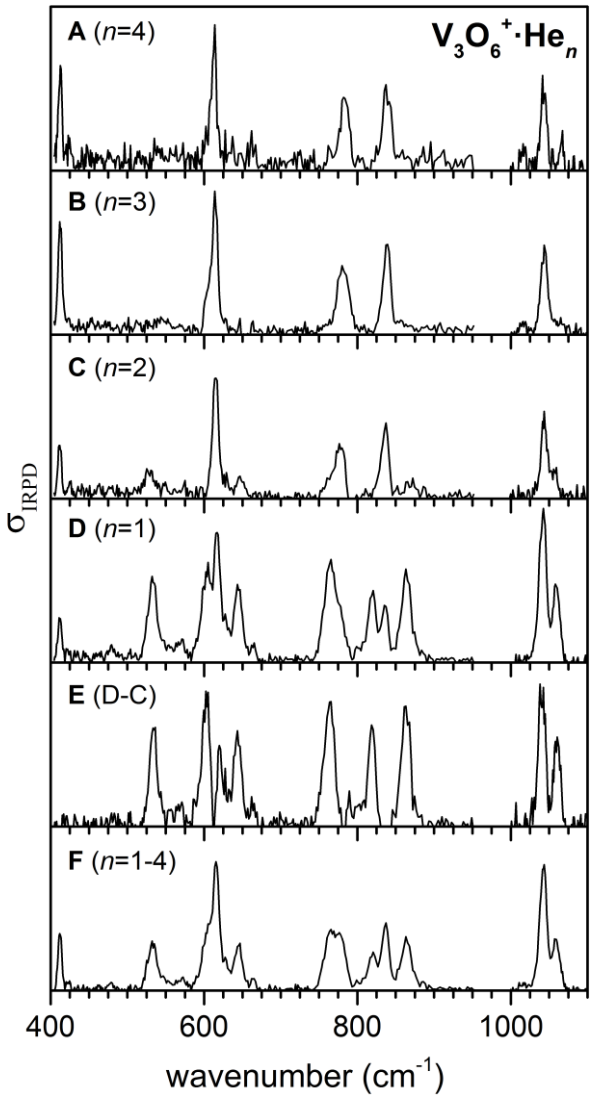

Figure S4: Experimental IRPD spectra of $V_3O_6^+ \cdot He_n$ complexes for different mass channels (parent ions) corresponding to n=4 to n=1 (labeled **A**-**D**) and the sum of all for channels n=1-4 (**F**). The IRPD spectra **A**-**C** mainly reflect the IR action spectrum of a single isomer, while spectra **D** and **F** contain contributions from this isomer as well as another one. Spectrum **E** reflects the IRPD spectrum of this other isomer and was obtained by scaling spectrum **C** by a constant factor and subtracting it from spectrum **D.**

3. Other IRPD spectra

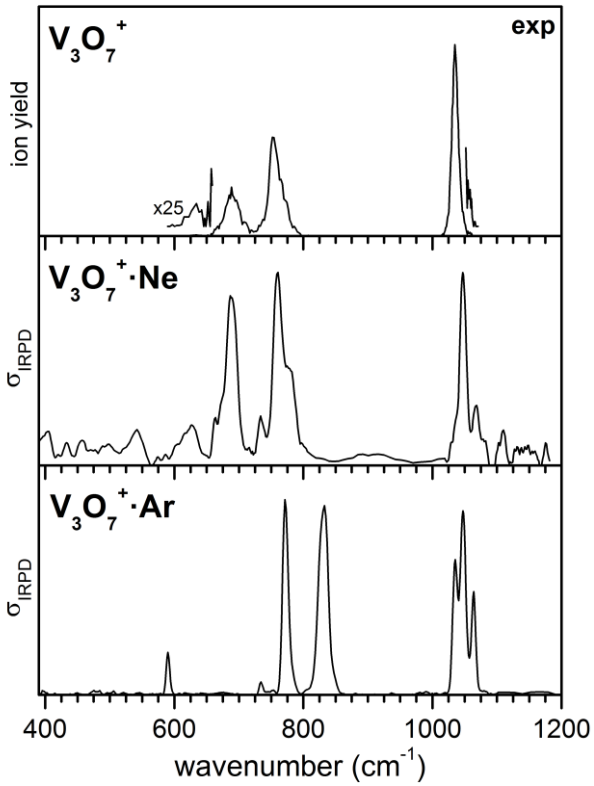

Figure S5: Experimental IRPD spectra of $V_3O_7^+$, $V_3O_7^+$·Ne, and $V_3O_7^+$·Ar in the region from 390 to 1200 cm^{-1}.